Article

The Real-Time Observation of Electric Vehicle Operating Points Using an Extended Kalman Filter

Younes Djellouli [1], Sid Ahmed El Mehdi Ardjoun [1,2,*], Emrah Zerdali [3], Mouloud Denai [4]
and Houcine Chafouk [2]

1   IRECOM Laboratory, Faculty of Electrical Engineering, Djillali Liabes University, Sidi Bel-Abbes 22000,
    Algeria; younes.djellouli@univ-sba.dz
2   IRSEEM/ESIGELEC Laboratory, Normandy University of Rouen, 76000 Rouen, France;
    houcine.chafouk@esigelec.fr
3   Department of Electrical and Electronics Engineering, Ege University, Izmir 35040, Türkiye;
    emrah.zerdali@ege.edu.tr
4   Higher School of Elecrical, Engineering and Energetics, Oran 31000, Algeria; denai_mouloud@esgee-oran.dz
*   Correspondence: elmehdi.ardjoun@univ-sba.dz

Abstract: Electric Vehicles (EVs) are set to play a crucial role in the energy transition. Although EVs offer significant environmental benefits, their technology still faces major challenges related to performance optimization, energy efficiency improvement, and cost reduction. A key point to address these challenges is the accurate identification of the speed/torque operating points of the drive systems. However, this identification is generally achieved using mechanical sensors, which are fragile, bulky, and expensive. This paper aims to develop, implement, and validate a speed/torque observer in real time based on the Extended Kalman Filter (EKF) approach for an EV equipped with an Open-End Winding Induction Motor with Dual Inverter (OEWIM-DI). The implementation of the EKF is based on the state modeling of the OEWIM-DI, enabling the observation of the torque and speed using voltage and current measurements. The validation of this approach is conducted experimentally on the FPGA and DS1104 boards. The results show that this approach offers excellent performance in terms of accuracy, stability, and real-time response speed. These results suggest that the proposed method could significantly contribute to the advancement of EV technology by providing a more robust and cost-effective alternative to traditional mechanical sensors while improving the overall efficiency and performance of EV drive systems.

Keywords: electric vehicle; open-end winding induction motor; dual inverter; extended Kalman filter; speed/torque observer; FPGA; DS1104

1. Introduction

Today, global industry is in the midst of an energy transition, driven by the need to reduce greenhouse gas emissions and combat climate change [1]. At the heart of this transition, Electric Vehicles (EVs) are emerging as the solution of the future, marking a major turning point in the transportation sector [2,3]. This rapid turnaround is encouraged by advances in EV technology and favorable government policies worldwide [4,5]. However, the development of EVs faces several challenges hindering their widespread adoption, such as optimizing performance, enhancing energy efficiency, and reducing both production and operating costs [6]. A crucial factor in overcoming these challenges is the accurate and real-time identification of EV speed/torque operating points [7].

Traditionally, speed and torque are measured directly using mechanical sensors [8–10]. However, the use of mechanical sensors has major drawbacks due to their complex installation as well as their fragility, size, and high cost [11,12]. This has a negative impact on the reliability, efficiency, and overall cost of EVs [13–16]. Given these constraints, numerous recent studies have focused on developing torque and speed observers, including the

Luenberger state observer [17], the sliding mode observer [18], and the Extended Kalman Filter (EKF) [19–22]. The EKF has proven to be a particularly promising observer for non-linear systems. As an extension of the classical Kalman filter, originally designed for linear systems, the EKF adapts to nonlinear systems by linearizing the state transition and observation models around the current state estimate [23]. Furthermore, it improves observation accuracy by combining system measurements with its mathematical model [24,25]. For instance, studies such as [26,27] focused on methods aimed at reducing periodic disturbances and attenuating velocity ripple. These disturbances can induce oscillations in speed and torque, adversely affecting the drive's performance and efficiency.

By addressing these issues, EKF-based methods enhance the precision of real-time control in systems where maintaining consistent torque and speed is critical, particularly in EV applications. Several studies, including [28–31], have demonstrated the EKF's capability to adaptively adjust torque and speed observations, even under disturbances and dynamic operating conditions. This adaptability is particularly beneficial in EVs, where conditions such as load, road gradient, and speed can change unpredictably [32]. The EKF's robustness in these dynamic conditions ensures smoother performance, reduces mechanical stress, and improves energy efficiency.

Speed estimation using an EKF is performed in two ways: under the infinite inertia assumption and with the aid of the equation of motion. The first approach assumes that the mechanical states change much more slowly than the electrical states, allowing for the assumption of constant speed during sampling intervals [24,28,29]. However, this method ignores the dynamics of the mechanical system, which can lead to degraded estimation performance at low speeds. To address this limitation, the second approach incorporates the equation of motion, which requires load torque information [19,20,22,23,31,32]. However, this information can be costly to measure and is often unavailable in many applications. Therefore, load torque is included as a joint state in the state vector, enabling it to be estimated alongside the other states. This method also enables the estimation of the viscous friction term as part of the load torque estimation. Consequently, the second approach improves speed estimation performance over a wide speed range and provides insights into the load within the system under control.

Another crucial aspect in the development of EVs is the energy conversion system. Induction motors have been widely adopted in EVs due to their numerous advantages, including simplicity of construction, reliability, robustness, low cost, and minimal maintenance requirements [33,34]. Their ability to provide a fast torque response and high efficiency in variable speed drives makes them especially well suited for EVs [35]. Several configurations exist for integrating power electronics into induction motors, and a particularly effective structure is presented in [36–39]. The innovative design involves opening up the neutral point of the stator windings, deviating from the conventional star/delta configuration. This approach allows each end of the windings to be supplied by an inverter with an independent or common DC source, creating a dual-inverter configuration. This configuration is known as an Open-End Winding Induction Motor with Dual Inverter (OEWIM-DI). The OEWIM-DI structure has received considerable attention for EVs. The unique features of this design offer multiple advantages in terms of power management, control flexibility [40], and fault tolerance [41,42]. Consequently, the OEWIM-DI configuration presents itself as a promising solution for EVs [7].

This paper focuses on the development, implementation, and real-time validation of an EKF-based speed and torque observer for an OEWIM-DI-driven EV. The originality of the proposed approach lies in the use of the EKF based on accurate state modeling of the OEWIM-DI. This method enables the estimation of EV torque and speed using only voltage and current measurements, thereby eliminating the need for additional mechanical sensors. To highlight the originality of the proposed approach, Table 1 presents a comparative literature review showcasing notable advancements in the identification of EV speed/torque operating points. The use of the EKF, which is the main focus of this paper, follows on from

this work, seeking to improve the accuracy and robustness of the real-time observation of speed/torque operating points. The contributions of this research are as follows:

- The development of an accurate state model of the OEWIM-DI;
- The design of an EKF for real-time speed and torque observation;
- The experimental implementation and validation of the observer on the FPGA and DS1104 boards.

Table 1. A literature review on the identification of speed/torque operating points.

Refs.	Application to EV	Motor Type	Mechanical Sensor	Real-Time Validation	Method Used	Evaluation Criteria		
						Cost	Volume/Size	Complexity
[43]	No	PMSM	Without	Yes	Extended Kalman Filter Observer	Medium	Medium	Medium
[44]	No	PMSM	Without	Yes	Sliding Model Observer	Medium	Medium	High
[45]	No	IM	With	Yes	Encoder Measurement	Medium	Medium	Medium
[46]	Yes	PM	With	Yes	Dynamometer Measurement	High	Medium	Medium
[47]	Yes	IM	With	Yes	Dynamometer Measurement	High	High	Medium
[48]	Yes	IM	With	No	Calculate Simulation	Medium	Medium	Medium
[49]	Yes	PMSM	Without	Yes	Recursive Least Square Estimator	Low	Low	Medium
[50]	Yes	DSIM	With	No	Calculate Simulation	High	High	Medium
[51]	No	IM	Without	Yes	Extended Kalman Filter Observer	Low	Low	Medium
[52]	Yes	SynRM	With	Yes	Encoder Measurement	High	High	Medium
Our work	EV New power train	OEWIM	Without	Yes	Extended Kalman filter Observer	Low	Low	Medium

The remainder of this paper is organized as follows: Section 2 introduces the EV system under study and presents the models of the system components. Section 3 details the methodology and design of the EKF. Section 4 presents the experimental setup and the tests carried out, followed by an in-depth discussion of the results. Finally, Section 5 concludes the paper with a summary of the key contributions and recommendations for future research directions.

2. The Modeling of the EV System Driven by an OEWIM-DI

This section first describes the forces exerted on the EV, followed by the power chain model. Finally, the mathematical model of an OEWIM in the stationary reference frame is presented.

2.1. A Model of the Forces Exerted on an EV

The modeling of EVs can be complex due to the nature of the system, which presents numerous interactions and dynamics that are difficult to characterize [15,53]. In this paper,

only the forces exerted on the EV are modeled, as illustrated in Figure 1, and the equations of the motion of the EV are presented in Table 2.
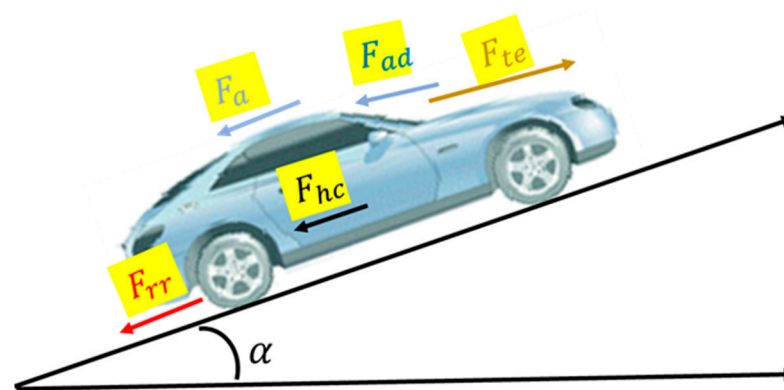
Figure 1. Elementary forces acting on a vehicle.

Table 2. EV equations of motion.

Quantity	Equation	
Rolling resistance	$F_{rr} = K_r m g$	(1)
Acceleration force	$F_a = ma + J_m \frac{G^2}{\eta_G R_W 2}\, a$	(2)
Slope force	$F_{hc} = \pm mg \sin \alpha$	(3)
Aerodynamic resistance	$F_{ad} = \frac{1}{2} A V^2 \rho C_d$	(4)
Mechanical equation for each drive wheel	$T_e = J_T \frac{dW_m}{dt} + K_f W_m + T_L$	(5)
Load torque	$T_L = R_w F_{te}$	(6)
Driving torque	$T_e = \frac{T_L}{G} = \frac{R_w F_{te}}{G}$	(7)
Total traction force	$F_{te} = F_{rr} + F_a + F_{hc} + F_{ad}$	(8)

2.2. Power Chain Model

Static converters play an essential role in the electrical architecture of EVs. These power electronic devices ensure the efficient management and conversion of energy between the battery and the electric motor. Figure 2 illustrates the powertrain topology of the EV considered in this paper.
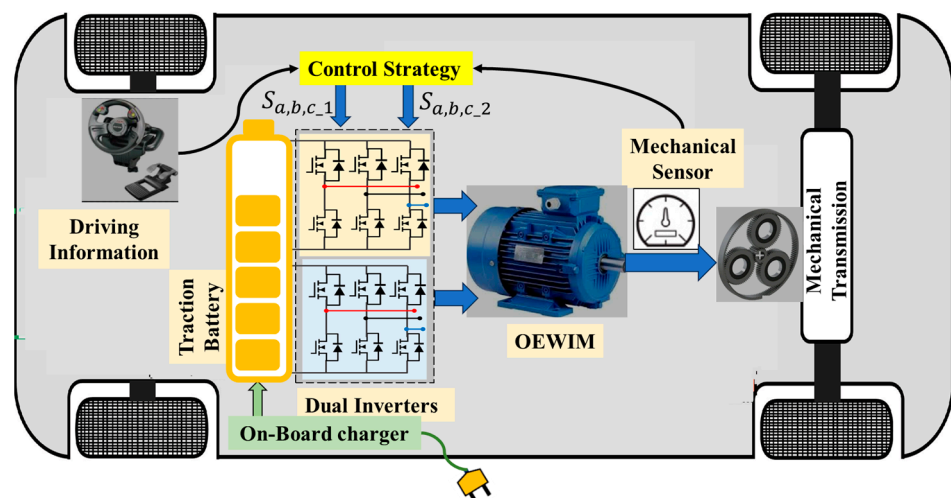
Figure 2. EV powertrain architecture.

The OEWIM and converter topology studied are illustrated in Figure 3. In this configuration, the OEWIM is fed by two dual-level inverters (indices i and j), with the converters

connected in parallel to a common DC voltage source. This configuration prevents over-loads without the need for additional equipment [36,54].
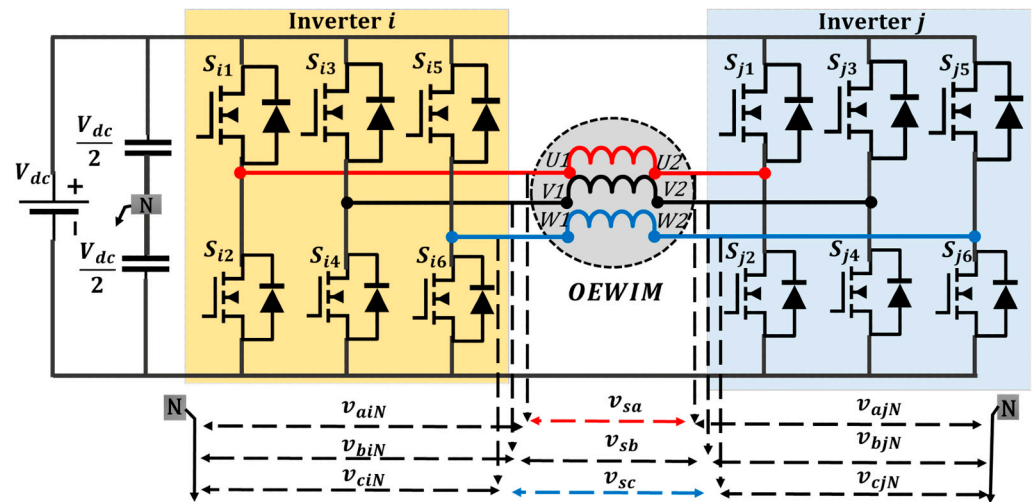
Figure 3. OEWIM dual-inverter structure using common DC source.

This configuration offers several advantages over conventional EV topologies. Firstly, this configuration allows for better power distribution between the two inverters, reducing stress on each component and improving the overall system's reliability [55]. Secondly, it offers greater flexibility in motor control, enabling finer optimization of performance and energy efficiency [56]. In addition, this topology can potentially reduce harmonics and electromagnetic noise, thus improving driving comfort [40]. The other advantage of this configuration is that if one of the inverters is faulty, the system will remain in operation but at a reduced power [57].

Figure 1 shows the possible voltage distribution vectors of inverters i and j feeding the first stator winding, consisting of six active vectors and two zero vectors depending on the inverter's switching state. Combining the two inverters gives a total ($2^3 \times 2^3 = 64$) and possible switching states ($2^3 = 8$ states for each inverter) [58].

In the configuration studied, the stator windings of the three motor phases are equally out of phase by a phase angle of $\vartheta = 120°$. These windings are supplied on both sides by the two dual-level inverters. This design eliminates the appearance of a homopolar current due to the connection path between the two inverters. The elimination of the zero sequence voltage plays a crucial role in suppressing this unwanted current [59,60].

This approach makes it possible to accurately analyze and quantify the phase voltages generated by the two inverters in the OEWIM system. By applying the electric circuit theory, it is possible to understand how the voltages are distributed in the various stator windings, thus providing a solid basis for the study and optimization of EV performance [61,62].

The phase voltages across each stator winding can be obtained according to Figure 3 as follows:

$$\begin{cases} v_{sa} = v_{aiN} - v_{ajN} \\ v_{sb} = v_{biN} - v_{bjN} \\ v_{sc} = v_{ciN} - v_{cjN} \end{cases} \tag{9}$$

with

$$\begin{cases} v_{aiN} = V_m cos(\omega t) \\ v_{biN} = V_m cos(\omega t - 120°) \\ v_{biN} = V_m cos(\omega t + 120°) \end{cases} \tag{10}$$

$$\begin{cases} v_{ajN} = V_m cos(\omega t + \vartheta) \\ v_{bjN} = V_m cos(\omega t - 120° + \vartheta) \\ v_{bjN} = V_m cos(\omega t + 120° + \vartheta) \end{cases} \tag{11}$$

2.3. A Mathematical Model of an OEWIM

The choice of induction machine model is aligned with the objectives and operating conditions of the studied system. Figure 4 shows a diagram of the equivalent circuit of the OEWIM transient dynamic model used in this paper [63].
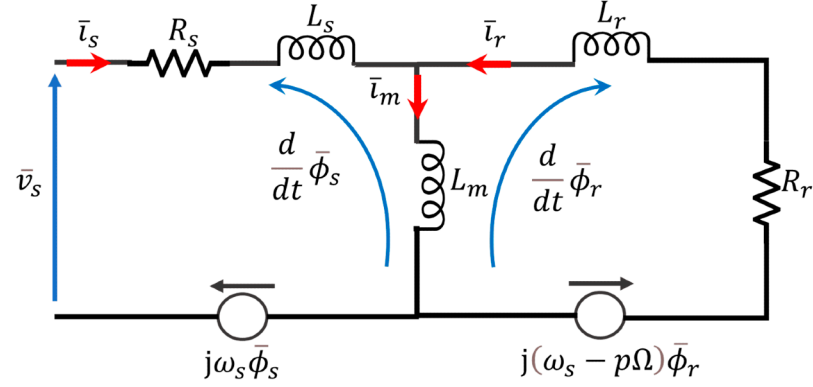
Figure 4. Diagram of OEWIM's transient dynamic equivalent circuit.

The dynamic behavior of the OEWIM can be represented mathematically by the following series of differential equations [64]:

Electrical equations for stator and rotor:

$$\begin{cases} \overline{v}_s = R_s\overline{i}_s + \frac{d}{dt}\overline{\phi}_s \\ \overline{v}_r = 0 = R_r\overline{i}_r + \frac{d}{dt}\overline{\phi}_r - \mathrm{j}(p\Omega)\overline{\phi}_r \end{cases} \tag{12}$$

Stator and rotor flux equations:

$$\begin{cases} \overline{\phi}_s = L_s\overline{i}_s + L_m\overline{i}_r \\ \overline{\phi}_r = L_r\overline{i}_r + L_m\overline{i}_s \end{cases} \tag{13}$$

Using the stationary reference frame (α, β), (12) and (13) can be rewritten as (14) and (15), respectively:

$$\begin{cases} v_{s\alpha} = R_s i_{s\alpha} + \frac{d}{dt}\phi_{s\alpha} \\ v_{s\beta} = R_s i_{s\beta} + \frac{d}{dt}\phi_{s\beta} \\ v_{r\alpha} = 0 = R_r i_{r\alpha} + \frac{d}{dt}\phi_{r\alpha} - p\Omega\phi_{r\beta} \\ v_{r\beta} = 0 = R_r i_{r\beta} + \frac{d}{dt}\phi_{r\beta} + p\Omega\phi_{r\alpha} \end{cases} \tag{14}$$

$$\begin{cases} \phi_{s\alpha} = L_s i_{s\alpha} + L_m i_{r\alpha} \\ \phi_{s\beta} = L_s i_{s\beta} + L_m i_{r\beta} \\ \phi_{r\alpha} = L_r i_{r\alpha} + L_m i_{s\alpha} \\ \phi_{r\beta} = L_r i_{r\beta} + L_m i_{s\beta} \end{cases} \tag{15}$$

The mechanical equations are given by

$$J\frac{d\Omega}{dt} = T_{em} - T_L - f_c\Omega \tag{16}$$

$$T_{em} = \frac{3}{2}p\left(\phi_{s\alpha}i_{s\beta} - \phi_{s\beta}i_{s\alpha}\right) \tag{17}$$

where v_r and v_s represent the rotor and stator voltages, respectively; i_r and i_s denote the components of rotor and stator current, respectively; ϕ_r and ϕ_s represent the flux components of the rotor and stator; R_r and R_s are the resistance of the rotor and stator; and L_r and L_s denote the rotor and stator inductances. L_m represents the mutual inductance, p denotes the number of pole pairs, and J stands for the inertia. The friction coefficient is denoted by f_c, and Ω represents the mechanical speed. The electromagnetic and load torques are denoted as T_{em} and T_L, respectively.

Thus, the state-space model of the machine is given as follows:

$$
\begin{bmatrix} \dot{i}_{s\alpha} \\ \dot{i}_{s\beta} \\ \dot{\phi}_{r\alpha} \\ \dot{\phi}_{r\beta} \\ \dot{\Omega} \end{bmatrix} = \begin{bmatrix} K_1 & 0 & K_2 & K_3\omega_r & 0 \\ 0 & K_1 & -K_3 & K_2 & 0 \\ K_4 & 0 & K_5 & -\omega_r & 0 \\ 0 & K_4 & \omega_r & K_5 & 0 \\ -K_6\phi_{r\beta} & K_6\phi_{r\alpha} & 0 & 0 & K_7 \end{bmatrix} \begin{bmatrix} i_{s\alpha} \\ i_{s\beta} \\ \phi_{r\alpha} \\ \phi_{r\beta} \\ \Omega \end{bmatrix} + \begin{bmatrix} K_8 & 0 \\ 0 & K_8 \\ 0 & 0 \\ 0 & 0 \\ 0 & 0 \end{bmatrix} \begin{bmatrix} v_{s\alpha} \\ v_{s\beta} \end{bmatrix} - \begin{bmatrix} 0 \\ 0 \\ 0 \\ 0 \\ K_9 \end{bmatrix} T_L \quad (18)
$$

where $K_1 = -\frac{1}{\sigma L_s}(R_s + \frac{L_m^2}{T_r L_r})$, $K_2 = \frac{1}{\sigma L_s}(\frac{L_m}{L_r T_r})$, $K_3 = \frac{1}{\sigma L_s}\left(\frac{L_m}{L_r}\right)$, $K_4 = \frac{L_m}{T_r}$, $K_5 = -\frac{1}{T_r}$, $K_6 = \frac{3}{2}\frac{p}{J}\frac{L_m}{L_r}$, $K_7 = -\frac{f_c}{J}$, $K_8 = \frac{1}{\sigma L_s}$, $K_9 = \frac{1}{J}$, $\omega_r = p\Omega$, and $T_r = \frac{R_r}{L_r}$.

The next section focuses on designing an EKF-based speed/torque observer utilizing an extended version of the model in (18).

3. Design of EKF-Based Speed/Torque Observer

The EKF is a mathematical tool that uses measurable physical quantities to estimate the system parameters, without the need for sensors, or when these parameters are not directly measurable. The EKF is adapted to stochastic systems, using system noise and the statistical characteristics of measurement noise to create a system with multiple inputs and outputs [30].

For the EKF implementation, the nonlinear equations of state can be represented by

$$
\begin{cases} \dot{x}_k = f(x_k, u_k) + w_k \\ y_k = h(x_k) + v_k \end{cases} \quad (19)
$$

where

x_k is the state vector.

u_k is the input vector.

y_k is the measurement vector.

w_k and v_k are the process and measurement noise, respectively, assumed to be Gaussian and zero-mean.

The simplified EFK is based on the linearization of the system around the estimated current state. This approach allows nonlinearities to be handled iteratively by updating the state and covariance estimates at each time step. The fundamental concept of EKF is described by the flowchart in Figure 5.
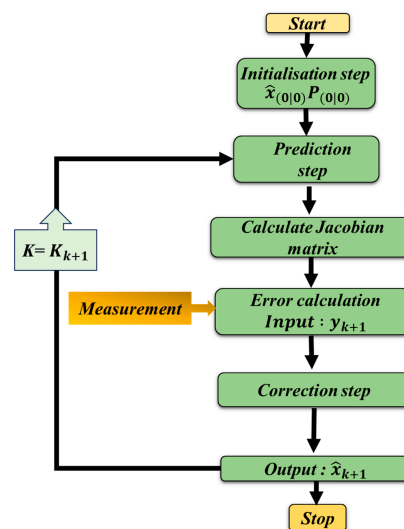
Figure 5. Basic steps in implementing the EFK algorithm.

The basic steps illustrated in Figure 5 are summarized as follows [23,51,65,66]:

a.   **Initialization**

Define $\hat{x}(0|0)$: the initial estimate of state;
Define P $(0|0)$: the initial error covariance matrix;
Define Q_k: the covariance matrix of process noise;
Define R: the measurement noise covariance matrix.
The covariance matrices Q_k and R are empirically tuned to balance the response speed and stability of the observer.

$$Q_k = \mathrm{diag}\left(\left[1e^{-2}1e^{-2}1e^{-2}1e^{-2}1e^{-2}1e^{-1}\right]\right) \tag{20}$$

$$R = \mathrm{diag}\left(\left[1e^{-2}1e^{-2}\right]\right) \tag{21}$$

b.   **Prediction**

The prediction step consists of estimating the state and covariance at time k + 1 using the system model.
Linearization:
To apply the EKF, the nonlinear functions *f* and *h* are linearized using a Taylor series expansion around the estimated state $\hat{x}_k$.
The Jacobian matrix of the state transition function is

$$F_k = \frac{df}{dx}\Big|_{\hat{x}_k, u_k} \tag{22}$$

The Jacobian matrix of the observation function is

$$H_k = \frac{dh}{dx}\Big|_{\hat{x}_k} \tag{23}$$

State prediction is carried out as follows:

$$\hat{x}_{k+1|k} = f(\hat{x}_k, u_k) \tag{24}$$

Covariance prediction is carried out as follows:

$$P_{k+1|k} = F_k P_k F_k^T + Q_k \tag{25}$$

c.   **Update or Correction:**

The update step adjusts the state estimate using the new measurements.
The Kalman gain is as follows:

$$K_{k+1} = P_{k+1|k}H_{k+1}^T\left(H_{k+1}P_{k+1|k}H_{k+1}^T + R_{k+1}\right)^{-1} \tag{26}$$

The status update is carried out as follows:

$$\hat{x}_{k+1|k+1} = \hat{x}_{k+1|k} + K_{k+1}\left[y_{k+1} - h\left(\hat{x}_{k+1|k}\right)\right] \tag{27}$$

The covariance update is carried out as follows:

$$P_{k+1|k+1} = \left[I - K_{k+1}H_{k+1}\right]P_{k+1|k} \tag{28}$$

where *I* is the identity matrix.
In our study, the EKF is used to observe the speed and torque of the EV. It relies solely on the measurements of stator currents and voltages while leveraging a nonlinear state model of the OEWIM. The EKF operates in two main stages: prediction and update.

- Prediction: At each instant *k*, the EKF uses the nonlinear model of the OEWIM to estimate the future states of the system, including speed and torque. This estimation is based on previously calculated states, system inputs (applied voltages), and a dynamic model of the motor.
- Update: Once new measurements of the stator currents and voltages are available, the EKF compares them to the values predicted using the model. This comparison determines a correction based on the difference between actual observations and initial estimates. The filter then adjusts its estimates to align with the real data, thereby improving the accuracy of the observed states.

A crucial aspect of the EKF is its ability to handle uncertainties inherent in measurements and models. For the OEWIM, process noise w_k (related to motor modeling) and measurement noise v_k (from current and voltage sensors) are incorporated into the estimation process. By accounting for these uncertainties, the EKF provides more robust estimates, even in the presence of disturbances or rapid changes in the motor's operating conditions.

The general formulation of the discretized model used by the EKF to represent the dynamics of the OEWIM can be expressed as follows (Figure 6) [24]:

$$\begin{cases} \hat{x}_{k+1} = A_d \hat{x}_k + B_d u_k + w_k \\ y_{k+1} = H \hat{x}_k + w_k \end{cases} \tag{29}$$

$$\hat{x}_k = \begin{bmatrix} \hat{i}_{s\alpha,k}, \hat{i}_{s\beta,k}, \hat{\phi}_{r\alpha,k}, \hat{\phi}_{r\beta,k}, \hat{\omega}_{r,k}, \hat{T}_{L,k} \end{bmatrix}^T \text{ and } u_k = \begin{bmatrix} u_{s\alpha,k} & u_{s\beta,k} \end{bmatrix}$$

$$A_d = \begin{bmatrix} 1 - K_1 T & 0 & K_2 T & K_3 T \omega_{r,k} & 0 & 0 \\ 0 & 1 - K_1 T & -K_3 T & K_2 T & 0 & 0 \\ K_4 T & 0 & 1 - K_5 T & -T\omega_{r,k} & 0 & 0 \\ 0 & K_4 T & T\omega_{r,k} & 1 - K_5 T & 0 & 0 \\ -K_6 T \phi_{r\beta,k} & K_6 T \phi_{r\alpha,k} & 0 & 0 & 1 - K_7 T & K_9 T \\ 0 & 0 & 0 & 0 & 0 & 1 \end{bmatrix}; B_d = \begin{bmatrix} K_8 T & 0 \\ 0 & K_8 T \\ 0 & 0 \\ 0 & 0 \\ 0 & 0 \\ 0 & 0 \end{bmatrix}; H = \begin{bmatrix} 1 & 0 \\ 0 & 1 \\ 0 & 0 \\ 0 & 0 \\ 0 & 0 \\ 0 & 0 \end{bmatrix}^T.$$

where *T* is the sampling time.
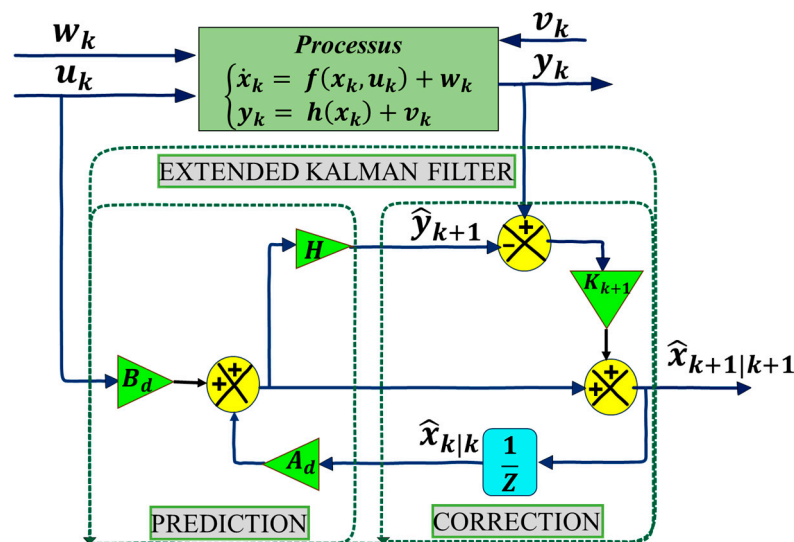
Figure 6. The structure of the EKF observer.

The next section first introduces the experimental setup used in real-time validation. Various tests were carried out on this test rig in order to demonstrate the effectiveness of the proposed EKF-based speed/torque observer for an EV application driven by an OEWIM-DI.

4. Real-Time Validation Results and Interpretation

The experimental test bench (Figure 7) used in this paper consists of a 1.5 kW OEWIM, driven by two inverters connected to a common DC bus source. This DC bus is connected to the grid via an autotransformer and a rectifier. The variable load of the OEWIM is obtained by adjusting the resistance of the DC generator. Appropriate current and speed sensors provide the necessary information to the controller, while the EV torque is calculated using the equations presented in Table 2.
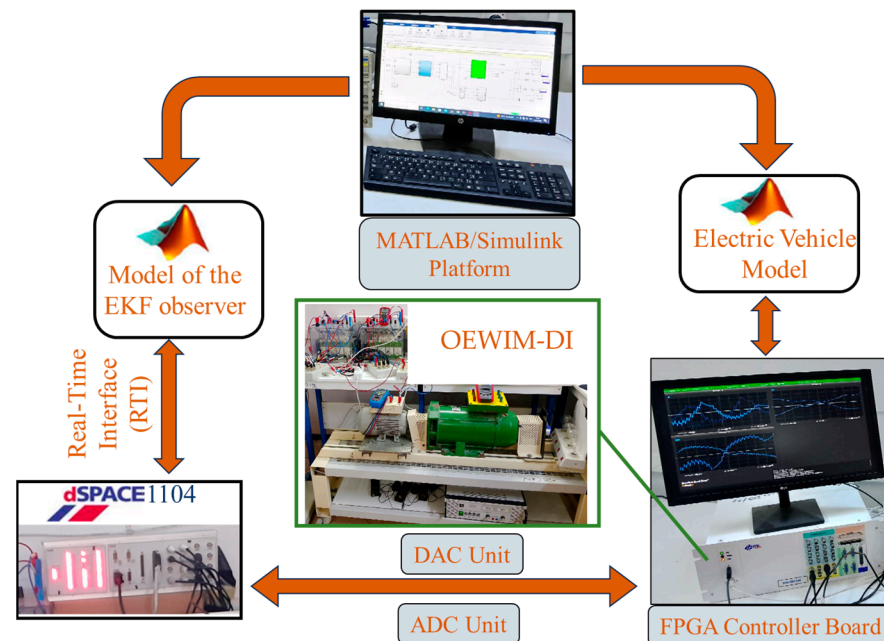
Figure 7. The experimental setup.

To further assess the robustness and performance of the EKF-based speed/torque observer for the OEWIM applied to EVs, a series of tests were carried out, such as variations in speed/torque operating points. The aim of these tests was to assess the system's ability to accurately track and adapt to changes in speed and torque under various dynamic driving patterns similar to those encountered in real life, as illustrated in Figure 8.
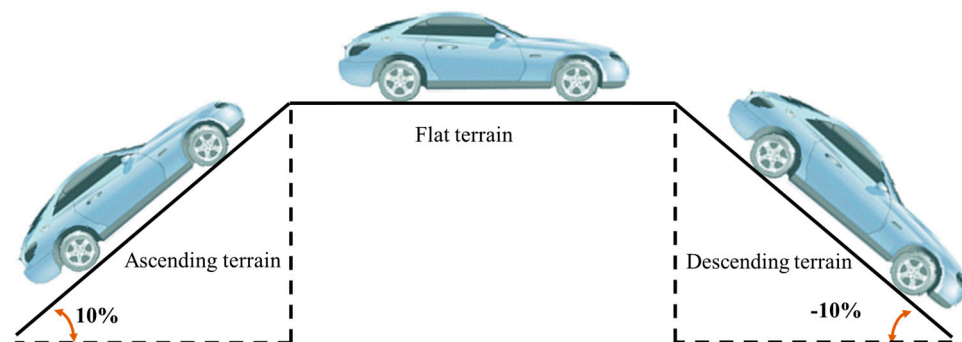
Figure 8. Proposed driving cycle for EV.

Real-time validation was carried out on an experimental setup developed by the authors. This experimental setup included a DS1104 and FPGA boards and an OEWIM-DI. The FPGA board was used to implement the EV model (Appendix A) and OEWIM-DI controls, while the DS1104 board was used to implement the EKF observer.

4.1. Test 1: Flat Terrain

In the first test, it was assumed that the EV was driving on a flat road. The speed profile applied consisted of the following phases: a 2 s stop phase, followed by an acceleration phase to 100 km/h, a 4 s stabilization phase, and, finally, a deceleration phase to 0 km/h, followed by another 2 s stability and stop phase. For the reverse speed, we started with the stop phase, followed by an acceleration phase to 100 km/h in 2 s, and then a stabilization phase of 4 s, followed by deceleration to 0 km/h in 2 s. The results obtained in the first test are illustrated in Figure 9. According to the results obtained in the first trial, we observed a very good match between the measured and observed quantities.
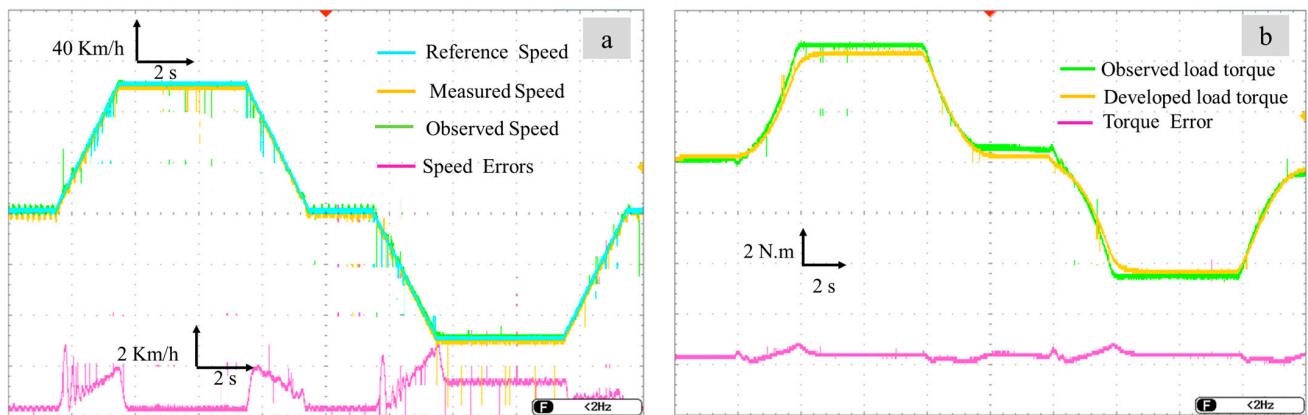
Figure 9. Test 1 results: (**a**) speeds; (**b**) torques.

4.2. Test 2: Inclined Terrain

In the second test, it was assumed that the EV was driving on a 10% slope. The same speed profile as that in the first test was applied (without introducing the reverse direction in this test). In this context, the EV can either go up or down this slope. The results of this test are shown in Figures 10 and 11. These results show a very good match between the measured and observed quantities whether the EV was ascending or descending.
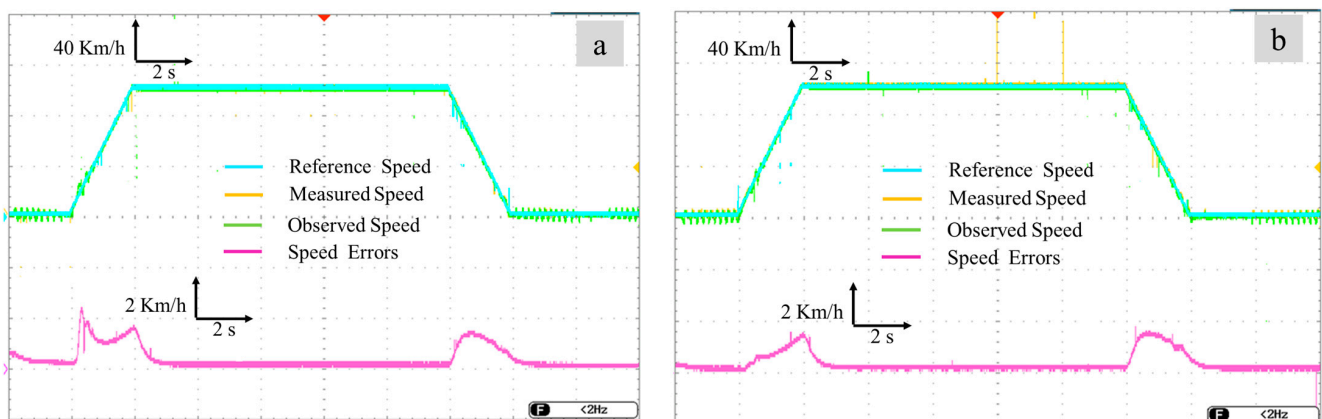
Figure 10. Speed rethinking during second test: (**a**) ascending; (**b**) descending.
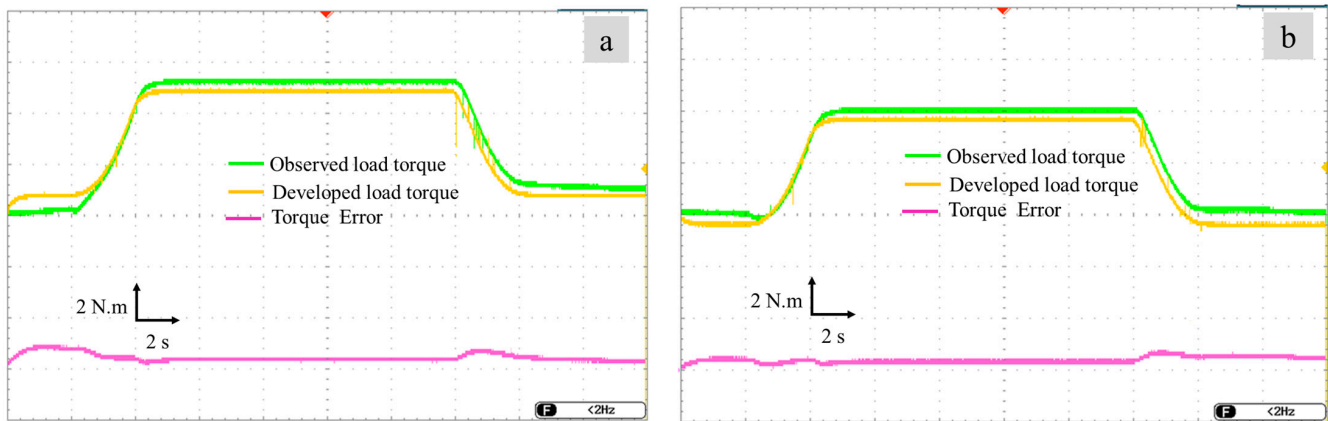
Figure 11. The couple's rethinking during the second trial: (**a**) ascending; (**b**) descending.

4.3. Test 3: Turning Behavior

This test allowed us to observe the behavior of the EV when making right and left turns at a constant vehicle speed (100 km/h).

At time t = 4 s, the EV begins the right turn at 100 km/h. In this scenario, the drive wheels travel different paths and rotate at different speeds, even though they are turning in the same direction. The inside drive wheel rotates at a lower speed, while the outside drive wheel rotates at a higher speed. The speeds are illustrated in Figure 12a,b. The electric differential adjusts the reference speed for each drive wheel, decreasing the speed for the right-drive wheel on the inside of the turn and increasing the speed for the left-drive wheel on the outside of the turn.
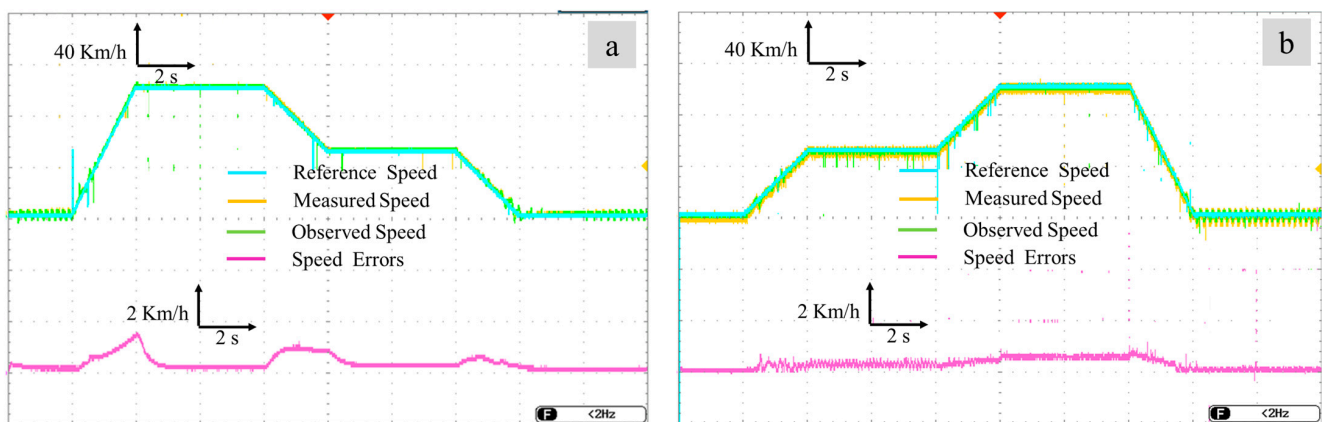
Figure 12. Speed response during test 3: (**a**) right turn; (**b**) left turn.

The analysis of a turn focuses on two key points: the entry, where speed is the most critical, and the apex, which represents the ideal trajectory for efficiently navigating the turn.

The torques experienced by the EV during this test are shown in Figure 13a,b. It can be observed that the aerodynamic torque mirrors the vehicle's speed.
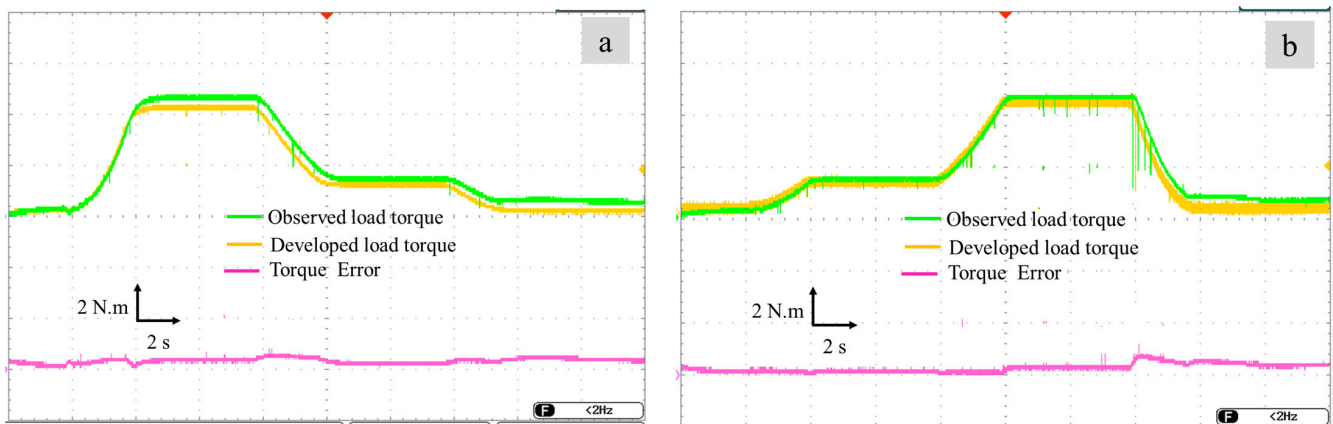
Figure 13. Torque response during test 3: (**a**) right turn; (**b**) left turn.

The primary goal of this test is to evaluate the vehicle's response and the stability of its traction system when subjected to significant lateral forces. This scenario highlights the challenges of maintaining tire grip and managing centrifugal forces. The data collected will help analyze the effectiveness of the torque and speed observer, as well as the robustness of the electric motor management system in the face of rapid changes in driving conditions.

5. Conclusions

In this paper, a novel approach based on a real-time EKF observer was proposed for the accurate identification of the speed/torque operating points of an EV traction system equipped with an OEWIM-DI. To implement the proposed method in real time, the EKF observer and EV model were deployed on a DS1104 controller board and an FPGA platform, respectively. The experimental results obtained from the developed test platform demonstrate that the observer reliably tracks speed and torque across a wide range of operating points, even under dynamically changing conditions. This real-time accuracy confirms that the proposed EKF observer effectively addresses a critical requirement for enhancing EV performance and efficiency, making it a valuable tool for improving EV control.

Several directions for future research have emerged from this study:

-   Adaptive Covariance Adjustment: Incorporating adaptive artificial intelligence-based methods to adjust the EKF's covariance matrix could dynamically improve the accuracy, particularly under variable conditions.
-   Comparative Studies: Conducting a comparative study with EV systems that apply a constant voltage–torque relationship will help evaluate the performance benefits and limitations of the EKF-based approach relative to conventional methods.
-   Continuous Parameter Refinement: Machine learning techniques can be utilized to refine the EKF observer's parameters in real time, potentially incorporating adaptive and heuristic algorithms for optimization.
-   Integration of Advanced Energy Management: Integrating the EKF observer with advanced energy management systems could further enhance the overall vehicle efficiency by optimizing power distribution and reducing energy loss in real-world driving conditions.

Overall, this work highlights the potential of EKF observers in enhancing EV performance and opens new avenues for future innovations in adaptive control and energy management within electric vehicle systems.

Nomenclature

F_{te}	Traction force (Newtons)
F_{rr}	Rolling resistance force (Newton)
F_a	Acceleration force (Newton)
F_{hc}	Hill climbing resistance (Newton)
F_{ad}	Aerodynamic drag force (Newton)
m	Vehicle mass (Kg)
g	Acceleration of gravity (N/m)
a	Vehicle acceleration (m/s^2)
J_m	Wheel inertia moment ($Kg.m^2$)
η_G	Gear efficiency (%)
R_W	Wheel radius (m)
ρ	Air density ($Kg.m^3$)
K_r	Tire rolling resistance coefficient
G	Gear ratio
C_d	Drag coefficient
v_S, v_r	Various stator/rotor voltages (V)
i_s, i_r	Various stator/rotor currents (A)
$\overline{\phi}_s, \overline{\phi}_r$	Various stator/rotor flux (Wb)
R_s, R_r	Various stator/rotor resistors (Ohm)
L_s, L_r	Various stator/rotor inductances (H)
L_m	Mutual inductance (H)
σ	Total leakage coefficient
J	Inertia ($Kg.m^2$)
p	Number of pole pairs
f_c	Friction coefficient ($N.m.s.rad^{-1}$)
Ω	Mechanical speed ($Rad.s^{-1}$)
T_{em}, T_L	Electromagnetic and load torques (N.m)
EV	Electric vehicle
OEWIM	Open-end winding induction motor
PMSM	Permanent magnet synchronous motor
PM	Permanent magnet
DSIM	Dual-star induction machine
SynRM	Synchronous reluctance motor
IM	Induction motor
DC	Direct current
EKF	Extended Kalman filter
DI	Dual inverter

Appendix A

The parameters of the EV used for real-time implementation.

Vehicle Parameters	
Specification	*Parameters*
m	*150 Kg*
g	*9.81 m/s^2*
R_W	*0.23 m*
ρ	*0.23 Kg/m^2*
G	*5*
C_d	*0.25*
A	*1 m*
μ	*0.015*
f_c	*0.00138 N.m.s.rad^{-1}*

References

1. Hassan, M.H.; Mohamed, E.M.; Kamel, S.; Ardjoun, S.A.E.M. Stochastic Optimal Power Flow Integrating with Renewable Energy Resources and V2G Uncertainty Considering Time-Varying Demand: Hybrid GTO-MRFO Algorithm. *IEEE Access* **2024**, *12*, 97893–97923. [CrossRef]
2. Hegazy, O.; Barrero, R.; Van Mierlo, J.; Lataire, P.; Omar, N.; Coosemans, T. An Advanced Power Electronics Interface for Electric Vehicles Applications. *IEEE Trans. Power Electron.* **2013**, *28*, 5508–5521. [CrossRef]
3. Benhammou, A.; Hartani, M.A.; Tedjini, H.; Rezk, H.; Al-Dhaifallah, M. Improvement of Autonomy, Efficiency, and Stress of Fuel Cell Hybrid Electric Vehicle System Using Robust Controller. *Sustainability* **2023**, *15*, 5657. [CrossRef]
4. Oubelaid, A.; Taib, N.; Rekioua, T.; Bajaj, M.; Yadav, A.; Shouran, M.; Kamel, S. Secure Power Management Strategy for Direct Torque Controlled Fuel Cell/Supercapacitor Electric Vehicles. *Front. Energy Res.* **2022**, *10*, 971357. [CrossRef]
5. Muduli, U.R.; Al Jaafari, K.; Behera, R.K.; Beig, A.R.; Al Hosani, K.; Alsawalhi, J.Y. Predictive Battery Soc Control for Dual Propulsion Differential Four Wheel Drive Electric Vehicle. In Proceedings of the 2021 IEEE Energy Conversion Congress and Exposition (ECCE), Vancouver, BC, Canada, 10–14 October 2021; pp. 1490–1495.
6. Roy, H.; Roy, B.N.; Hasanuzzaman, M.; Islam, M.S.; Abdel-Khalik, A.S.; Hamad, M.S.; Ahmed, S. Global Advancements and Current Challenges of Electric Vehicle Batteries and Their Prospects: A Comprehensive Review. *Sustainability* **2022**, *14*, 16684. [CrossRef]
7. Younes, D.; El Mehdi, A.S.A.; Houcine, C.; Mouloud, D. Sensorless Torque Control of an Electric Vehicle Driven by an Open End Winding Induction Motor: An Experimental Study. In Proceedings of the 2023 Second International Conference on Energy Transition and Security (ICETS), Adrar, Algeria, 12–14 December 2023; pp. 1–6.
8. Pop, A.A. Incremental Encoder Speed Acquisition Using an STM32 Microcontroller and NI ELVIS. *Sensors* **2022**, *22*, 5127. [CrossRef]
9. Younes, D.; El Mehdi, A.S.A.; Mouloud, D.; Houcine, C. Real-Time Implementation of the Luenberger Torque Observer for an Induction Motor. In Proceedings of the 2023 2nd International Conference on Electronics, Energy and Measurement (IC2EM), Medea, Algeria, 28–29 November 2023; Volume 1, pp. 1–4.
10. Ferreira, F.J.; Lopes, F.J. Webcam-Based Tachometer for in-Field Induction Motor Load Estimation. In Proceedings of the 2016 XXII International Conference on Electrical Machines (ICEM), Lausanne, Switzerland, 4–7 September 2016; pp. 2380–2388.
11. Bahloul, M.; Chrifi-Alaoui, L.; Vargas, A.N.; Chaabane, M.; Drid, S. Online Robust Estimation of Flux and Load Torque in Induction Motors. *Int. J. Adv. Manuf. Technol.* **2018**, *94*, 2703–2713. [CrossRef]
12. Abbasi, M.A.; Husain, A.R.; Idris, N.R.N.; Anjum, W.; Bassi, H.; Rawa, M.J.H. Predictive Flux Control for Induction Motor Drives with Modified Disturbance Observer for Improved Transient Response. *IEEE Access* **2020**, *8*, 112484–112495. [CrossRef]
13. Kirchner, E.; Wallmersperger, T.; Gwosch, T.; Menning, J.D.M.; Peters, J.; Breimann, R.; Kraus, B.; Welzbacher, P.; Küchenhof, J.; Krause, D.; et al. A Review on Sensor-Integrating Machine Elements. *Adv. Sens. Res.* **2024**, *3*, 2300113. [CrossRef]
14. Bin Ahmad, M.S.; Pesyridis, A.; Sphicas, P.; Mahmoudzadeh Andwari, A.; Gharehghani, A.; Vaglieco, B.M. Electric Vehicle Modelling for Future Technology and Market Penetration Analysis. *Front. Mech. Eng.* **2022**, *8*, 896547. [CrossRef]
15. Ukaew, A. Model Based System Design for Electric Vehicle Conversion. In *New Trends in Electrical Vehicle Powertrains*; IntechOpen: London, UK, 2018.
16. Garcia, M.; Panagiotou, P.A.; Antonino-Daviu, J.A.; Gyftakis, K.N. Efficiency Assessment of Induction Motors Operating under Different Faulty Conditions. *IEEE Trans. Ind. Electron.* **2018**, *66*, 8072–8081. [CrossRef]

17. Zorgani, Y.A.; Koubaa, Y.; Boussak, M. MRAS State Estimator for Speed Sensorless ISFOC Induction Motor Drives with Luenberger Load Torque Estimation. *ISA Trans.* **2016**, *61*, 308–317. [CrossRef] [PubMed]

18. Barambones, O.; Alkorta, P. Position Control of the Induction Motor Using an Adaptive Sliding-Mode Controller and Observers. *IEEE Trans. Ind. Electron.* **2014**, *61*, 6556–6565. [CrossRef]

19. Zerdali, E. A Comparative Study on Adaptive EKF Observers for State and Parameter Estimation of Induction Motor. *IEEE Trans. Energy Convers.* **2020**, *35*, 1443–1452. [CrossRef]

20. Barut, M.; Demir, R.; Zerdali, E.; Inan, R. Real-Time Implementation of Bi Input-Extended Kalman Filter-Based Estimator for Speed-Sensorless Control of Induction Motors. *IEEE Trans. Ind. Electron.* **2011**, *59*, 4197–4206. [CrossRef]

21. Auger, F.; Hilairet, M.; Guerrero, J.M.; Monmasson, E.; Orlowska-Kowalska, T.; Katsura, S. Industrial Applications of the Kalman Filter: A Review. *IEEE Trans. Ind. Electron.* **2013**, *60*, 5458–5471. [CrossRef]

22. Yildiz, R.; Barut, M.; Zerdali, E. A Comprehensive Comparison of Extended and Unscented Kalman Filters for Speed-Sensorless Control Applications of Induction Motors. *IEEE Trans. Ind. Inform.* **2020**, *16*, 6423–6432. [CrossRef]

23. Nosheen, T.; Ali, A.; Chaudhry, M.U.; Nazarenko, D.; Shaikh, I.U.H.; Bolshev, V.; Iqbal, M.M.; Khalid, S.; Panchenko, V. A Fractional Order Controller for Sensorless Speed Control of an Induction Motor. *Energies* **2023**, *16*, 1901. [CrossRef]

24. Jayaramu, M.L.; Suresh, H.N.; Bhaskar, M.S.; Almakhles, D.; Padmanaban, S.; Subramaniam, U. Real-Time Implementation of Extended Kalman Filter Observer with Improved Speed Estimation for Sensorless Control. *IEEE Access* **2021**, *9*, 50452–50465. [CrossRef]

25. Abbas, M.; Chafouk, H.; Ardjoun, S.A.E.M. Fault Diagnosis in Wind Turbine Current Sensors: Detecting Single and Multiple Faults with the Extended Kalman Filter Bank Approach. *Sensors* **2024**, *24*, 728. [CrossRef]

26. Oubelaid, A.; Kakouche, K.; Belkhier, Y.; Khosravi, N.; Taib, N.; Rekioua, T.; Bajaj, M.; Rekioua, D.; Tuka, M.B. New Coordinated Drive Mode Switching Strategy for Distributed Drive Electric Vehicles with Energy Storage System. *Sci. Rep.* **2024**, *14*, 6448. [CrossRef] [PubMed]

27. Oubelaid, A.; Taib, N.; Rekioua, T.; Bajaj, M.; Blazek, V.; Prokop, L.; Misak, S.; Ghoneim, S.S. Multi Source Electric Vehicles: Smooth Transition Algorithm for Transient Ripple Minimization. *Sensors* **2022**, *22*, 6772. [CrossRef] [PubMed]

28. Benhamida, I.; Ameur, A.; Kouzi, K.; Gaoui, B. Torque Ripple Minimization in Predictive Torque Control Method of PMSM Drive Using Adaptive Fuzzy Logic Modulator and EKF Estimator. *J. Control. Autom. Electr. Syst.* **2019**, *30*, 1007–1018. [CrossRef]

29. Chebaani, M.; Mahmoud, M.M.; Tazay, A.F.; Mosaad, M.I.; Nouraldin, N.A. Extended Kalman Filter Design for Sensorless Sliding Mode Predictive Control of Induction Motors without Weighting Factor: An Experimental Investigation. *PLoS ONE* **2023**, *18*, e0293278. [CrossRef]

30. Ameid, T.; Menacer, A.; Talhaoui, H.; Harzelli, I. Rotor Resistance Estimation Using Extended Kalman Filter and Spectral Analysis for Rotor Bar Fault Diagnosis of Sensorless Vector Control Induction Motor. *Measurement* **2017**, *111*, 243–259. [CrossRef]

31. Yildiz, R.; Barut, M.; Demir, R. Extended Kalman Filter Based Estimations for Improving Speed-sensored Control Performance of Induction Motors. *IET Electr. Power Appl.* **2020**, *14*, 2471–2479. [CrossRef]

32. Zerdali, E.; Demir, R. Speed-Sensorless Predictive Torque Controlled Induction Motor Drive Withfeed-Forward Control of Load Torque for Electric Vehicle Applications. *Turk. J. Electr. Eng. Comput. Sci.* **2021**, *29*, 223–240. [CrossRef]

33. Miloudi, H.; Miloudi, M.; Ardjoun, S.A.E.M.; Mahmoud, M.M.; Telba, A.A.; Denaï, M.; Khaled, U.; Ewias, A.M. Electromagnetic Compatibility Characterization of Start-Capacitor Single-Phase Induction Motor. *IEEE Access* **2024**, *12*, 2313–2326. [CrossRef]

34. Ardjoun, S.A.E.M.; Abıd, M.; Aıssaouı, A.G.; Tahour, A. A Robust Sliding Mode Control Applied to the Double Fed Induction Machine. *IU-J. Electr. Electron. Eng.* **2012**, *12*, 1445–1451.

35. El Hadraoui, H.; Zegrari, M.; Chebak, A.; Laayati, O.; Guennouni, N. A Multi-Criteria Analysis and Trends of Electric Motors for Electric Vehicles. *World Electr. Veh. J.* **2022**, *13*, 65. [CrossRef]

36. Zerdani, M.; Ardjoun, S.A.E.M.; Chafouk, H.; Denaï, M. Experimental Investigation of Decoupled Discontinuous PWM Strategies in Open-End Winding Induction Motor Supplied by a Common DC-Link. *IEEE J. Emerg. Sel. Top. Power Electron.* **2023**, *11*, 3087–3096. [CrossRef]

37. Huang, Z.; Yang, T.; Giangrande, P.; Galea, M.; Wheeler, P. Technical Review of Dual Inverter Topologies for More Electric Aircraft Applications. *IEEE Trans. Transp. Electrif.* **2021**, *8*, 1966–1980. [CrossRef]

38. Muduli, U.R.; Beig, A.R.; Behera, R.K.; Al Jaafari, K.; Alsawalhi, J.Y. Predictive Control with Battery Power Sharing Scheme for Dual Open-End-Winding Induction Motor Based Four-Wheel Drive Electric Vehicle. *IEEE Trans. Ind. Electron.* **2021**, *69*, 5557–5568. [CrossRef]

39. Zerdani, M.; Chafouk, H.; Ardjoun, S.A.E.M. Performance Analysis of a Dual-Inverter-Fed Open-End Winding Induction Machine under Asymmetrical Control: Theoretical Approach and Experimental Validation. *Symmetry* **2024**, *16*, 395. [CrossRef]

40. Jia, Y.-F.; Xu, N.; Chu, L.; Zhang, Y.; Xu, Z.; Li, Y.-K.; Yang, Z.-H. Control Strategy for an Open-End Winding Induction Motor Drive System for Dual-Power Electric Vehicles. *IEEE Access* **2020**, *8*, 8844–8860. [CrossRef]

41. Chakrabarti, A.; Saha, A.; Biswas, S.K. Winding Open-circuit Fault-tolerant Operation of Single DC-link Dual-inverter Fed Three-phase Open-end Induction Motor Drive. *IET Power Electron.* **2021**, *14*, 1256–1270. [CrossRef]

42. Khadar, S.; Kouzou, A.; Rezaoui, M.M.; Hafaifa, A. Fault-Tolerant Sensorless Sliding Mode Control by Parameters Estimation of an Open-End Winding Five-Phase Induction Motor. *Meas. Control* **2019**, *92*, 6–15. [CrossRef]

43. Niewiara, Ł.; Tarczewski, T.; Grzesiak, L.M. Application of Extended Kalman Filter for Estimation of Periodic Disturbance and Velocity Ripple Reduction in PMSM Drive. *Bull. Pol. Acad. Sciences. Tech. Sci.* **2020**, *68*, 983–995. [CrossRef]

44. Boughezala, H.H.; Laroussi, K.; Khadar, S.; Al-Sumaiti, A.S.; Mossa, M.A. Optimized Sensorless Control of Five-Phase Permanent Magnet Synchronous Motor Using a Genetic Algorithm-Real Time Implementation. *IEEE Access* **2024**, *12*, 98367–98378. [CrossRef]

45. Ebrahim, O.S.; Badr, M.A.; Elgendy, A.S.; Jain, P.K.; Shawky, K.O. Neural Network Based Robust Optimal Energy Control of Pulse Width Modulation-inverter Fed Motor Driving Pump. *IET Electr. Power Appl.* **2023**, *17*, 1334–1346. [CrossRef]

46. Roshandel, E.; Mahmoudi, A.; Kahourzade, S.; Yazdani, A.; Shafiullah, G.M. Losses in Efficiency Maps of Electric Vehicles: An Overview. *Energies* **2021**, *14*, 7805. [CrossRef]

47. Roshandel, E.; Mahmoudi, A.; Soong, W.L.; Kahourzade, S. Optimal Design of Induction Motors over Driving Cycles for Electric Vehicles. *IEEE Trans. Veh. Technol.* **2023**, *72*, 15548–15562. [CrossRef]

48. Dianati, B.; Kahourzade, S.; Mahmoudi, A. Optimization of Axial-Flux Induction Motors for the Application of Electric Vehicles Considering Driving Cycles. *IEEE Trans. Energy Convers.* **2020**, *35*, 1522–1533. [CrossRef]

49. Lee, T.; Nam, K. Torque Control Based Speed Synchronization for Two-Speed Gear Electric Vehicle. *IEEE Access* **2021**, *9*, 153518–153527. [CrossRef]

50. Benbouya, B.; Cheghib, H.; Chrenko, D.; Delgado, M.T.; Hamoudi, Y.; Rodriguez, J.; Abdelrahem, M. Sliding Mode Control of an Electric Vehicle Driven by a New Powertrain Technology Based on a Dual-Star Induction Machine. *World Electr. Veh. J.* **2024**, *15*, 155. [CrossRef]

51. Miloud, I.; Cauet, S.; Etien, E.; Salameh, J.P.; Ungerer, A. Real-Time Speed Estimation for an Induction Motor: An Automated Tuning of an Extended Kalman Filter Using Voltage–Current Sensors. *Sensors* **2024**, *24*, 1744. [CrossRef]

52. Ghadbane, H.E.; Barkat, S.; Houari, A.; Djerioui, A.; Rezk, H.; Louzazni, M. Optimal Adaptive Fractional Order Integral Sliding Mode Controller-Energy Management Strategy for Electric Vehicles Based on Bald Eagle Search Algorithm. *Int. J. Energy Res.* **2024**, *2024*, 1–22. [CrossRef]

53. Benhammou, A.; Tedjini, H.; Guettaf, Y.; Soumeur, M.A.; Hartani, M.A.; Hafsi, O.; Benabdelkader, A. Exploitation of Vehicle's Kinetic Energy in Power Management of Tow-Wheel Drive Electric Vehicles Based on ANFIS DTC-SVM Comparative Study. *Int. J. Hydrogen Energy* **2021**, *46*, 27758–27769. [CrossRef]

54. Belkhode, S.; Jain, S. Optimized Switching PWM Technique with Common-Mode Current Minimization for Five-Phase Open-End Winding Induction Motor Drives. *IEEE Trans. Power Electron.* **2018**, *34*, 8971–8980. [CrossRef]

55. Lee, K.; Han, Y. Simple Discontinuous Pulse-Width Modulation Scheme for the Loss Reduction of a Dual Inverter Fed an Open-End Winding Induction Motor. *IEEE Trans. Energy Convers.* **2022**, *38*, 495–506. [CrossRef]

56. Mizukoshi, A.; Haga, H. Control Method for Reducing the Motor Loss of Dual-Inverter Fed Open-End Winding Induction Motor in the Low-Speed Region. *IEEJ J. Ind. Appl.* **2020**, *9*, 27–35. [CrossRef]

57. Fan, Y.; Cui, R.; Zhang, A. Torque Ripple Minimization for Inter-Turn Short-Circuit Fault Based on Open-Winding Five Phase FTFSCW-IPM Motor for Electric Vehicle Application. *IEEE Trans. Veh. Technol.* **2019**, *69*, 282–292. [CrossRef]

58. Khadar, S.; Kouzou, A.; Hafaifa, A. Sensorless Direct Torque Control of Induction Motor with an Open-End Stator Winding Using an Adaptive Luenberger Observer. In Proceedings of the 2018 15th International Multi-Conference on Systems, Signals & Devices (SSD), Yasmine Hammamet, Tunisia, 19–22 March 2018; pp. 1355–1362.

59. Yu, Z.; Gan, C.; Ni, K.; Chen, Y.; Qu, R. A Simplified PWM Strategy for Open-Winding Flux Modulated Doubly-Salient Reluctance Motor Drives with Switching Action Minimization. *IEEE Trans. Ind. Electron.* **2022**, *70*, 2241–2253. [CrossRef]

60. Edpuganti, A.; Rathore, A.K. Optimal Pulsewidth Modulation for Common-Mode Voltage Elimination Scheme of Medium-Voltage Modular Multilevel Converter-Fed Open-End Stator Winding Induction Motor Drives. *IEEE Trans. Ind. Electron.* **2016**, *64*, 848–856. [CrossRef]

61. Saad, K.; Abdellah, K.; Ahmed, H.; Iqbal, A. Investigation on SVM-Backstepping Sensorless Control of Five-Phase Open-End Winding Induction Motor Based on Model Reference Adaptive System and Parameter Estimation. *Eng. Sci. Technol. Int. J.* **2019**, *22*, 1013–1026. [CrossRef]

62. Mizukoshi, A.; Haga, H. Reduction of Voltage Harmonics in an Open-End Winding Induction Motor Driven by a Dual-Inverter with Floating-Capacitor in the Low-Speed Region. In Proceedings of the 2020 IEEE Energy Conversion Congress and Exposition (ECCE), Detroit, MI, USA, 11–15 October 2020; pp. 2656–2661.

63. Le Roux, P.F.; Ngwenyama, M.K. Static and Dynamic Simulation of an Induction Motor Using Matlab/Simulink. *Energies* **2022**, *15*, 3564. [CrossRef]

64. Zerdani, M.; Ardjoun, S.E.; Chafouk, H.; Denai, M. Experimental Validation of a New Power Chain for Electric Vehicles. In Proceedings of the 2022 2nd International Conference on Innovative Research in Applied Science, Engineering and Technology (IRASET), Meknes, Morocco, 3–4 March 2022; pp. 1–6.

65. Moaveni, B.; Masoumi, Z.; Rahmani, P. Introducing Improved Iterated Extended Kalman Filter (IIEKF) to Estimate the Rotor Rotational Speed, Rotor and Stator Resistances of Induction Motors. *IEEE Access* **2023**, *11*, 17584–17593. [CrossRef]

66. Farasat, M.; Karaman, E.; Trzynadlowski, A.M.; Fadali, M.S. Hybrid Field Orientation and Direct Torque Control for Electric Vehicle Motor Drive with an Extended Kalman Filter. In Proceedings of the 2012 IEEE Energytech, Cleveland, OH, USA, 29–31 May 2012; pp. 1–6.